Chapter-6

Effect of Sintering Temperature on the Structural, Dielectric, Ferroelectric, Piezoelectric and Optical Properties of Sm/Ta Co-Doped $Bi_4Ti_3O_{12}$ Aurivillius Piezoceramics

CHAPTER 6

Effect of Sintering Temperature on the Structural, Dielectric, Ferroelectric, Piezoelectric and Optical Properties of Sm/Ta Co-Doped $Bi_4Ti_3O_{12}$ Aurivillius Piezoceramics

6.1 Introduction

Among the extensively researched advanced functional materials, Aurivillius oxides have emerged as a remarkable class of compounds owing to their multifunctional properties and potential applications in a wide range of cutting-edge technologies [249]. PZT-based materials typically operate below 200 °C, which suffices for numerous industrial uses, yet there is a growing demand for piezoelectric materials that demonstrate stability at higher temperatures, particularly in sectors such as the military, metallurgy, and deep earth exploration [43]. This requirement underlines the importance of innovating piezoelectric substances that can withstand elevated temperatures. Bismuth layered structural ferroelectrics (BLSFs) emerge as promising candidates for such applications owing to their high Curie temperatures, T_C (exceeding 500 °C) [250], [251]. Among BLSFs, $Bi_4Ti_3O_{12}$ (BIT), a member of the Aurivillius family, characterized by a layered perovskite-like structure has garnered significant attention in recent years. Its intriguing structural features and unique electrical, ferroelectric, and piezoelectric properties have spurred extensive research aimed at harnessing its full potential for applications in high-temperature transducers, sensors, resonators and filters [252]. Additionally, BIT ceramics have exhibited potential in photocatalysis, photoconductivity supercapacitors, FeRAM, optical displays, sensors, and non-volatile resistive switching devices [253]. The appeal lies in their substantial T_C, reaching approximately ~675 °C, coupled with notable piezoelectric coefficients that surpass those of quartz single crystals. BIT is characterized by its distinctly anisotropic monoclinic layered structure, featuring a sequence of

alternating atomic configurations [254]. This structure comprises two pseudo-perovskite $(Bi_2Ti_3O_{10})^{2-}$ layer and a single bismuth oxide $(Bi_2O_2)^{2+}$ layer arranged periodically along the c-axis, connected with an additional oxygen plane [255], [256], [257], [258]. In BIT, the spontaneous polarization is predominantly along the a-axis. This polarization results primarily from the movement of cations relative to oxygen ions in the perovskite layers [254], [259], [260]. In BIT single crystals, a substantial spontaneous polarization of 50 $\mu C/cm^2$ has been observed along the a-axis, with a smaller polarization of 4 $\mu C/cm^2$ noted along the c-axis [260]. Due to its elevated transition temperature, BIT ceramics show promise for applications in high-temperature piezoelectrics. However, a significant challenge in practical piezoelectric use arises from the relatively poor piezoelectric properties, high conductivity and lower electrical resistivity of BIT. The electrical conductivity in BIT exhibits a marked anisotropy, with the highest values occurring in the plane parallel to the polarization direction. These ceramics are recognized for their exceptionally high electrical conductivity within the ab plane, surpassing that along the c-axis by roughly an order of magnitude. At higher temperatures, the predominant defects are intrinsic oxygen vacancies, whereas at lower temperatures, electron holes emerge as the main carriers, resulting in the deterioration of electrical properties. Therefore, successful poling of BIT ceramics is challenging. A key hurdle for BIT-based materials is to attain high electrical resistivity. The high electrical resistivity of the piezoceramic serves two important purposes: first, it enables the application of a high poling field, which helps in polarizing the ceramic and achieving high piezoelectric properties; second, it reduces charge leakage, especially at high temperatures. Investigations have demonstrated that targeted doping at the A-site and/or B-site of the $(Bi_2Ti_3O_{10})^{2-}$ units within BIT ceramics can markedly enhance their electrical resistivity, along with boosting their ferroelectric and piezoelectric attributes.

The dielectric and ferroelectric characteristics of bismuth compounds can be modulated through the substitution of ions on the A and/or B sites within the perovskite-like layers, utilizing ions with suitable ionic radii and valences [261], [262], [263]. Some studies shows A-site substitution has edge over B-site substitution due to higher tolerance, making it more feasible [264]. Integrating rare earth elements into BIT through doping enhances its stability and functional properties, as this method substitutes volatile bismuth ions, reducing both bismuth and oxygen vacancies and influencing its electrical polarization [265]. As a result, modified BIT ceramics exhibit superior ferroelectric, dielectric, and luminescent characteristics [266]. In an earlier study, doping of Sm^{3+} ions in BIT increased the dielectric constant, likely due to induced distortion in the TiO_6 octahedra due to altered electronic interactions within the lattice. Moreover, the presence of Sm^{3+} ions effectively hinder the volatilization of bismuth and reduces defects within the crystal structure. This dual effect contributes synergistically to the overall increase in the dielectric constant of the material [267]. A-site La-doped BIT films have been documented to exhibit an enhanced P_r of 12 $\mu C/cm^2$, along with superior fatigue properties [268]. Conversely, aliovalent substitution using donor cations, such as V^{5+}, Nb^{5+}, Sb^{5+}, Ta^{5+}, and W^{6+} at B site have been an effective approach as it decrease electrical conductivity by few orders of magnitude compared to undoped variant, while significantly boosting the piezoelectric charge coefficient d_{33} to 16–40 pC/N [269], [270], [271], [272], [273]. This enhancement can be primarily attributed to donor doping at the B-site, which lowers oxygen vacancies or electron hole concentrations via charge compensation effects, and creates greater deviations in the rigid structure along the a-direction of the $[B_mO_{3m+1}]$ part of the perovskite block. Additionally, recent research has shown that co-doping with W/Mn and W/Nb in Aurivillius ceramics improves resistivity (10^{11} Ωcm), enhances d_{33} (21 pC/N), and decreases dielectric loss compared to solely W-

doped counterparts, making these materials well-suited for pyroelectric and piezoelectric devices [274]. Moreover, Mn/Ta co-doping has led to materials that exhibit a d_{33} value of 31 pC/N highlighting the beneficial impact of strategic doping with multiple dopants on the electrical properties of BIT-based compounds [250].

In this Chapter, both the A and B sites substitutions were employed incorporating the rare earth ion Sm^{3+} at the A site and the donor ion Ta^{5+} in the BIT lattice, resulting in a nominal composition of $(Bi_{4-x}Sm_{0.5})(Ti_{3-0.01}Ta_{0.01})O_{12}$. The investigation comprehensively analyzed the effects of doping and sintering temperature variations on various properties including crystal structure, microstructure, morphology, dielectric, ferroelectric, piezoelectric, and optical characteristics. The results demonstrated significant improvements in piezoelectric, ferroelectric, and dielectric properties for BITST S1150, attributed to enhanced resistivity and decreased oxygen vacancies, highlighting its potential for high-temperature applications.

6.2 Experimental Details

6.2.1 Sample Preparation

The pure $Bi_4Ti_3O_{12}$ and $(Bi_{4-x}Sm_{0.5})(Ti_{3-0.01}Ta_{0.01})O_{12}$ ceramics were synthesized using the high energy ball milling method through the conventional mixed oxide route. High-purity reagents, namely Bi_2O_3 (Sigma Aldrich 99.9%), TiO_2 (Sigma Aldrich 99%), Sm_2O_3 (Alfa aesar 99.9%), and Ta_2O_3 (Sigma Aldrich 99%), were measured stoichiometrically and placed in a zirconia jar in ethanol media with zirconia balls for high energy ball milling (Restch Germany) for 24 hours at 150 rpm. The resulting slurry was dried overnight in an oven at 100 ºC. The collected powder was then calcined at 850 ºC for two hours. Subsequently, the calcined powder was mixed with 2 wt. % PVA, serving as a binding agent, and pressed into pellets with a diameter of 10 mm and a thickness of approximately

1 mm. The pure $Bi_4Ti_3O_{12}$ (BIT) pellets were sintered in a closed environment at 950 ºC for 4 hours, with the inclusion of spacer powder to offset Bi evaporation during the high-temperature heat treatment. Notably, when the sintering temperature for Pure BIT was increased up to 1150 °C, significant melting was observed. From this, we can deduce that Sm/Ta doping aids in expanding the sintering temperature window. The Sm/Ta-doped BIT, abbreviated as BITST, underwent sintering at varying temperatures of 950 °C, 1050 °C, and 1150 °C for 4 hours each. They are designated as BITST S950, BITST S1050, and BITST S1150 based on the respective sintering temperatures, and the abbreviations are self-explanatory. Archimedes setup was utilized to measure the density of the sintered pellets. To alleviate unnecessary strain generated during crushing, the sintered pellets were crushed to form powder, followed by annealing at 500 °C for 12 hours.

6.2.2 Characterizations

The crystal structural characterization of the prepared samples was done using benchtop X-ray diffractometer (Rigaku Miniflex 600, Japan). The confirmation of phase formation was conducted through Fourier transform infrared spectroscopy (FTIR) in transmission mode at ambient temperature in KBr mode with 64 scans and a resolution of 4 cm^{-1}, employing the Nicolet iS5 THERMO Electron Scientific Instruments LLC, USA. XRD data were structurally examined through Le-Bail profile matching and Rietveld structural refinement using 'FullProf Suite' software. Microstructural analysis of gold-coated sintered pellets was performed employing a scanning electron microscope (FEI Quanta 200 F). The flat pellet surfaces underwent polishing and were subsequently coated with platinum and silver paste for electrical characterization. Curing of the platinum paste and silver electroded pellets took place at 950 °C and 550 °C for 30 minutes, each respectively. Temperature-dependent dielectric constant ($\varepsilon_r(T)$) and loss tangent (tan $\delta(T)$), across a frequency range of 20 Hz to 10 MHz were measured using an impedance analyzer

(Keysight E4990A, Agilent software). These measurements were made in a computerized furnace that maintained a temperature change rate of 3 °C per minute, within a range of 30 °C to 700 °C. Ferroelectric hysteresis (P-E) loops, along with measurements of current response, leakage current, resistivity, and PUND were conducted at 10 Hz and 50 Hz AC signals using the Precision Premier LC II ferroelectric loop tracer from Radiant Technologies, USA. For the piezoelectric evaluations, the samples underwent poling at temperatures ranging from 100 to 200 °C for 15 minutes within a silicone oil bath, subjected to a DC electric field of 20-40 kV/cm. The piezoelectric charge coefficient (d_{33}) was determined using the Berlincourt quasistatic d_{33} meter PIEZOTEST (UK), applying a force of 0.25 N and at a frequency of 110 Hz. X-ray photoelectron spectroscopy (XPS) analyses using the Thermo Scientific K-Alpha equipment were conducted to investigate the chemical states of Fe and O. The UV-Vis spectrophotometer (UV-2600, Shimadzu) was used for diffuse reflectance spectroscopy to measure the band gaps of the prepared samples. The photoluminescence measurement was done using Fluorescence Spectrophotometer (F-4600, Hitachi). These analyses collectively provided a comprehensive understanding of the structural, dielectric, ferroelectric, piezoelectric, and optical properties of the investigated ceramic samples based on BIT.

6.3 Results and Discussion

6.3.1 Structural Analysis

6.3.1.1 Crystal Structural Analysis

The room temperature powder XRD patterns of pure BIT ceramic sintered at 950 °C and Sm, Ta codoped BIT ceramic sintered at 950 °C, 1050 °C and 1150 °C, all for four hours and subsequently annealed at 500 °C for 12 hours are depicted in Figure 6.1. All the primary peaks observed in the powder XRD data matches well with the JCPS No. 72-

1019 representing the parent $Bi_4Ti_3O_{12}$ compound with B2cb space group and orthorhombic crystal symmetry [275]. Sm^{3+} (1.09 Å) ions, with a radius ranging from 1.1 to 1.3 Å, have the potential to replace Bi^{3+} ions (1.34 Å) within the perovskite layer. Similarly, Ta^{5+} ions, with a radius falling within the range of 0.58 to 0.65 Å, can substitute for Ti^{4+} ions (0.605 Å) in the octahedral site. The lower limit in both cases is governed by the stability of the perovskite layer, while the upper limit is determined by the mismatch between the Bi-O and perovskite layers [264]. This confirms the successful incorporation of Sm/Ta into BIT lattice and formation of pure phase without the presence of any reactant impurity or secondary phase formation.

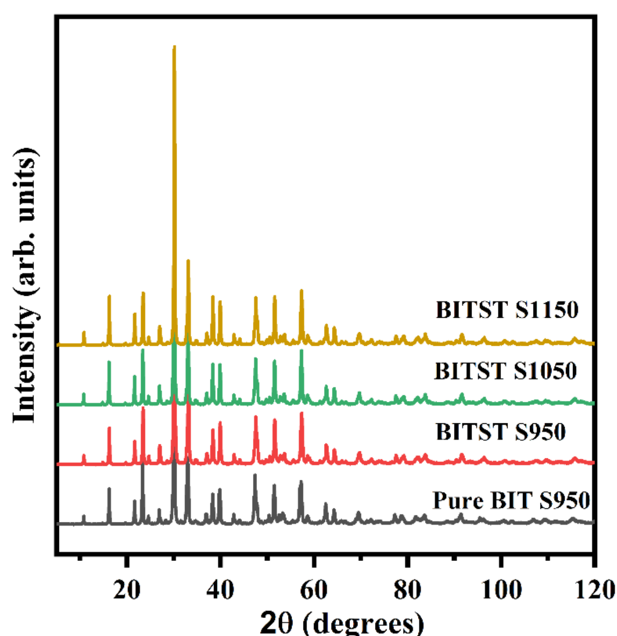

Figure 6.1 Powder XRD patterns at room temperature of pure BIT and Sm/Ta co-doped BIT at various sintering temperatures.

To further understand the crystal structure, Lebail fitting and Rietveld refinement was performed on the powder XRD data using Fullprof suite. Figure 6.2 shows the well-fitted Rietveld refined patterns for Pure BIT, BITST S950, BITST S1050 and BITST S1150.

For Rietveld refinement the space group B2cb (41) was used, and the lattice parameters and the refinement parameters are given in Table 6.1.

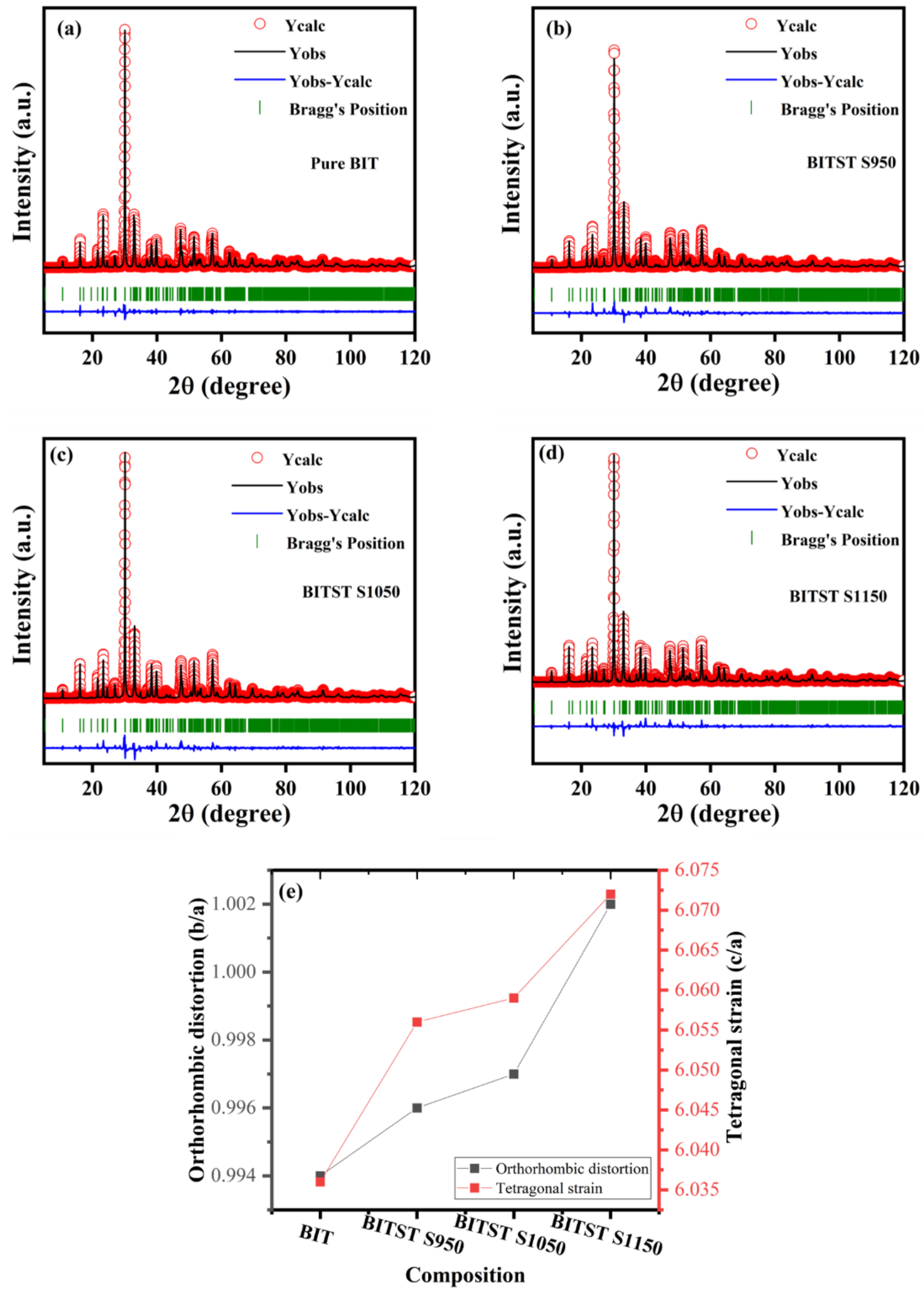

Figure 6.2 Rietveld Refined patterns for (a) Pure BIT, (b) BITST S950, (c) BITST S1050 (d) BITST S1150 and (e) orthorhombic distortion and tetragonal strain variation with composition.

The alterations in the structure of BLSFs ceramics can be ascertained through the examination of structural distortion parameters. Incorporation of Sm/Ta to BIT leads

to an enhancement in the orthorhombic distortion (b/a), which initially measured 0.994 for Pure BIT but rose to 1.002 for BITST S1150. Moreover, elevating the sintering temperature from 950 °C to 1150 °C in Sm/Ta doped BIT results in an increment in the overall orthorhombic distortion [267].

Table 6.1 Table for lattice parameters and refined parameters obtained from Rietveld refinement for Pure BIT and BITST sintered at 950 °C, 1050 °C and 1150 °C.

Composition	**BIT**	**BITST S950**	**BITST S1050**	**BITST S1150**
Crystal System	Orthorhombic	Orthorhombic	Orthorhombic	Orthorhombic
Space Group	B2cb (41)	B2cb (41)	B2cb (41)	B2cb (41)
Lattice Parameters Å	a=5.4454(7) b=5.4110(7) c=32.8678(1)	a= 5.4220(5) b = 5.4021(3) c= 32.8349(6)	a= 5.4241(7) b = 5.4097(9) c= 32.8633(3)	a =5.4072(6) b=5.4164(5) c=32.8342(4)
Refinement parameters	R_p = 8.47 R_{wp} = 13.9 χ^2 = 3.34	R_p = 10.3 R_{wp} = 14.8 χ^2 = 4.99	R_p = 12.0 R_{wp} = 17.2 χ^2 = 6.84	R_p = 8.43 R_{wp} = 12.9 χ^2 = 3.26
Orthorhombic distortion (b/a)	0.994	0.996	0.997	1.002
Tetragonal strain (c/a)	6.036	6.056	6.059	6.072

6.3.1.2 Fourier Transform Infrared (FTIR) Analysis

Figure 6.3 illustrates the FTIR spectra corresponding to both pristine BIT and Sm/Ta substituted BIT samples sintered at 950 °C, 1050 °C and 1150 °C. The spectra reveal several significant absorption features indicative of the chemical composition and

structural characteristics of the materials. The broad absorption peak observed in the spectral range of 3300-3700 cm^{-1} across all samples corresponds to the antisymmetric and symmetric stretching vibrations of hydroxyl (OH) groups and water molecules. Additionally, a distinct peak at approximately 1632 cm^{-1} is attributed to the bending vibration of water molecules [189], [224]. An absorption band around 2923 cm^{-1} is identified, arising from the stretching vibrations of OH^- groups. The presence of this band is ascribed to the hygroscopic property of the pottasium bromide powder utilized in pellet formation, as no distinctive peak is detected in the range of 1000-4000 cm^{-1} [190]. Furthermore, two prominent absorption bands are observed: one approximately at 815 cm^{-1} and the other at around 660 cm^{-1} respectively corresponding to the Bi-O stretching vibration and the Ti-O stretching vibration [253]. These bands serve as distinctive signatures for the confirmation of perovskite structure in BIT-based materials [253].

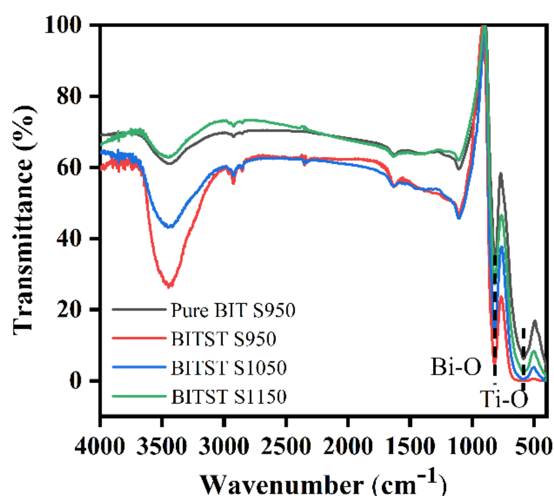

Figure 6.3 FTIR spectra for Pure BIT, BITST S950, BITST 1050 and BITST S1150 measured in KBr mode.

6.3.1.3 X-ray Photoelectron Spectroscopy Analysis

Core-level photoemission spectra were obtained to understand the valence states of the Oxygen, Bismuth, and Titanium present in the Pristine BIT and Sm/Ta co-doped BIT (BITST S1150) materials. Figure 6.4 (a,b) displays the Bi 4f, Bi 5d, Ti 2p, O 1s, Sm 3d and Ta 4f core-level photoemissions, confirming the presence of all the respective elements [276]. Furthermore, no additional peaks arising from other elements or impurities were observed, confirming the high purity of the samples. The XPS binding energy scale was corrected for charge using standard calibration methods, with the C-1s peak serving as a reference point fixed at 284.8 eV via CASA XPS software. Regarding structural properties, vacancies such as ($V_{Bi}^{'''}$) and ($V_{O}^{\bullet\bullet}$) may occur within the perovskite layers because of the volatility of Bi during the sintering process, underscoring the critical importance of XPS studies [277]. The nuclear-level photoemission of asymmetric O1s peak is deconvoluted into three component peaks as shown in Figure 6.5. The O-1s spectrum was fitted using an Asymmetric Lorentzian (LA) function overlaid on a Shirley background. The LA function, resembling a Voigt-like function, encompasses a generalized Lorentzian function combined with a Gaussian function to account for both peak asymmetry and Gaussian characteristics, ensuring accurate XPS fitting. The peak situated at a lower binding energy of ~529 eV is commonly associated with lattice O^{2-} ions. The literature indicates, the peaks observed at higher binding energy of 531 eV (O_V) were presumably arising from the to O^{-} /O^{2-} ions generated as a result of loss of oxygen or the generation of oxygen vacancies [278]. Conversely, the peak at ~532 eV (O_{ads}) is attributed to the adsorption of OH on the surface of the samples [195], [224], [279], [280], [281]. To compare the difference in oxygen vacancies in the pure BIT and BITST S1150 samples, the ratio of area of the component peak of oxygen vacancies (~531 eV) to lattice oxygen (~529

eV peak) are calculated. The Sm/Ta doped BIT samples sintered at 1150 °C are found to contain fewer oxygen vacancies, with ratios of oxygen vacancies ($V_O^{\bullet\bullet}$) of 51:49 and 34:66 for pure BIT and BITST S1150 samples, respectively for Figure 6.5 (a) and 6.5 (b). As depicted in Figure 6.6 (a-b) the Bi $4f_{7/2}$ and Bi $4f_{5/2}$ components of the Bi 4f spin-orbit doublet are positioned at 158.72 eV and 164.02 eV, and at 158.71 eV and 164.01 eV, in pure BIT and BITST S1150, respectively. The observed spin-orbit splitting energy of 5.3 eV, derived from the binding energy level spectrum of the two primary peaks, closely aligns with the values documented in the literature for Bi $4f_{7/2}$ and Bi $4f_{5/2}$. This consistency in the binding energy serves to further validate the experimental data [67]. Defects, notably bismuth and oxygen vacancies are acknowledged as the most mobile charges in perovskites. They increase the electrical conductivity which has detrimental affect on overall functional properties. Sm/Ta co-doping might be attributed to improved density owing to enhanced sinterability and reduced concentrations of oxygen vacancies resulting from volatilization through defect reactions. Figure 6.7 depicts the core level spectra of Ti 2p state for pure BIT and BITST S1150. The Ti 2p XPS spectra exhibited intensity maxima for Ti $2p_{3/2}$ and Ti $2p_{1/2}$ for pure BIT at 457.6 eV and 463.2 eV and for BITST S1150 at 457.8 eV and 463.5 eV, respectively [278], [282]. This observation underscores the presence of Ti ions exists in a +4 valence state within the perovskite layer of bismuth titanate [250], [276], [283], [284]. The peaks approximately at 459.6 eV and 471 eV are satellites peak as they are on the higher binding energy to Ti^{4+} might be attributed to shakeup process [285], [286]. The broadened peak at around 465 eV can be deconvoluted into two component peaks one situated approximately at 463 eV attributed to Ti $2p_{1/2}$ photoemission peak and other at 465 eV attributed to Bi $4d_{3/2}$ core level peak [250], [283].

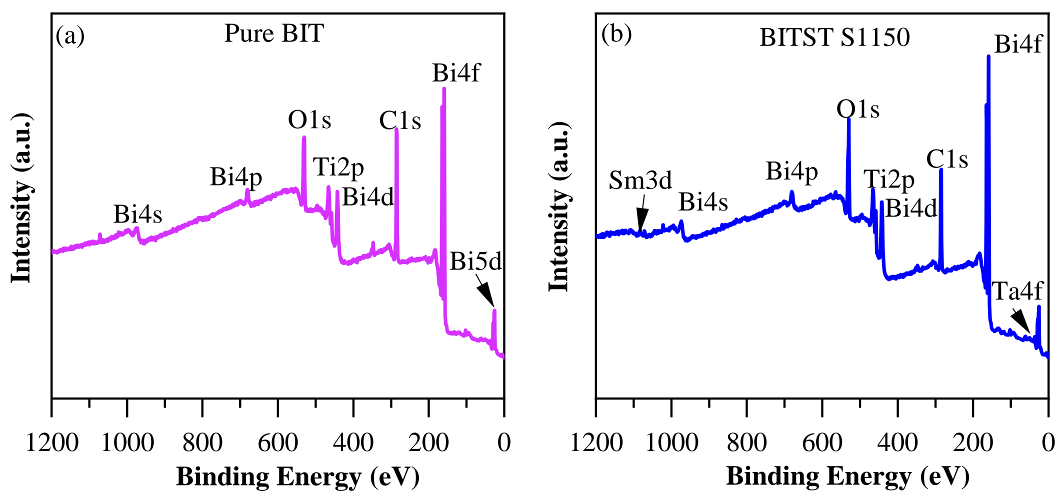

Figure 6.4 Full XPS spectrum of Pure BIT and BITST S1150.

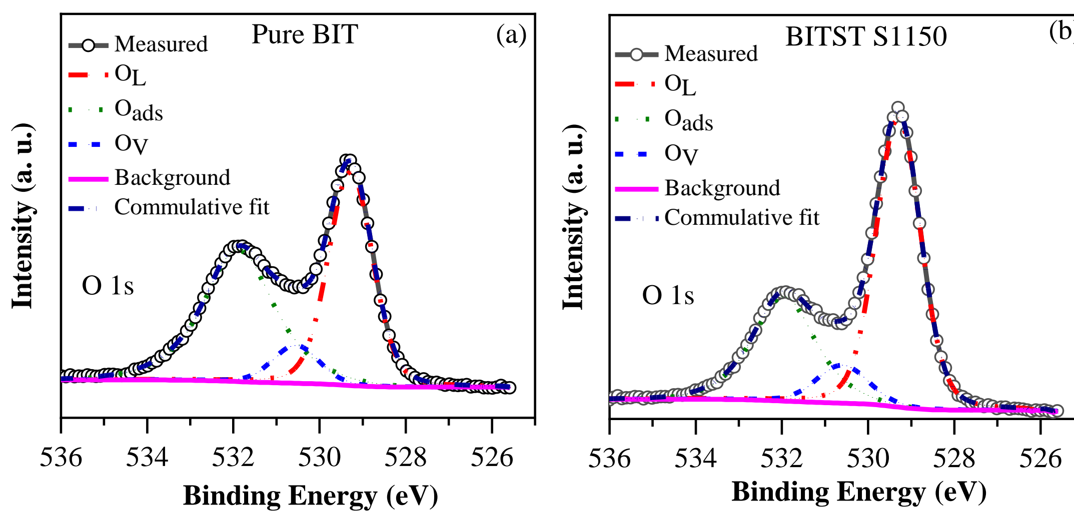

Figure 6.5 XPS spectra of O 1s for Pure BIT and BITST S1150.

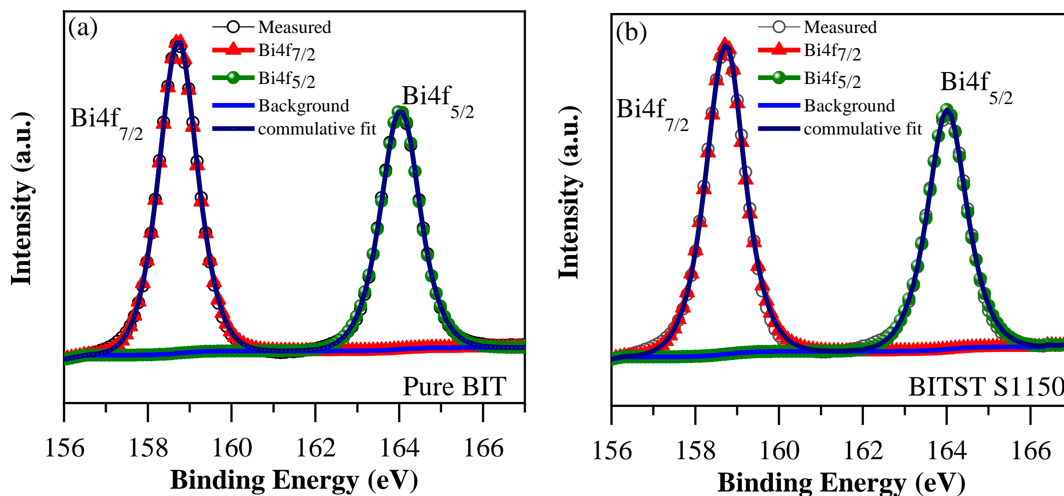

Figure 6.6 XPS spectra of Bi 4f for Pure BIT and BITST S1150.

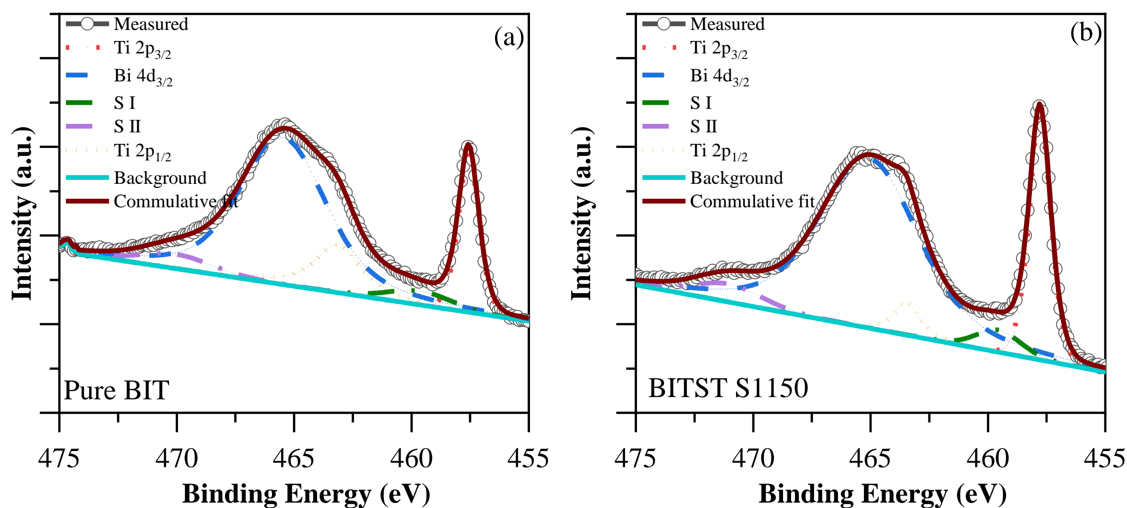

Figure 6.7 XPS spectra of Ti 2p for Pure BIT and BITST S1150.

6.3.2 Microstructural Studies

The SEM micrographs of gold sputtered pellet surface for pure BIT and Sm, Ta co-doped BIT sintered at 950 °C, 1050 °C and 1150 °C are shown in Figure 6.8. SEM micrographs reveal a dense microstructure with clear grain boundaries. Because of the

anisotropic nature of crystal structure, all ceramic specimens display a distinctive lamellar crystal structure typical of BLSFs [250]. The randomly orientated small platelet like microstructure is obtained in the samples sintered at lower temperature (950 °C, 1050 °C) which grew significantly at higher temperature (~1150 °C), consistent with the previous literature [273], [283]. The intriguing emergence of plate-like grains is attributed to the unique anisotropic nature inherent in the crystal structures of Aurivillius compounds [273]. The average thickness of these platelets was calculated using Image J software. Noteworthy is the variation in the average grain/platelet thickness, ranging from 0.5 µm (Pure BIT) to 2.4 µm (BITST S1150) which increases with increasing temperature indicating the combined effects of doping and temperature enhances grain growth along the a-b plane, resulting in larger platelets as shown in Figure 6.9. On increasing the sintering temperature, the dense microstructure is obtained with negligible porosity. The Figure 6.10 (a-b) shows the elemental mapping confirming the uniform distribution of all the elements present in both pristine BIT and Sm/Ta co-doped BIT. The successful diffusion of Sm and Ta into BIT lattice can be confirmed through this. The EDAX spectrum depicted in Figure 6.10 (c) verifies the presence of three elements: Bi, Ti, and O in BIT, whereas Figure 6.10 (d) confirms the presence of Sm, Ta, Bi, Ti, and O. Nonetheless, the incorporation of Sm/Ta doping adds an intriguing dimension, as it triggers a decrease in grain size. This phenomenon implies that Sm/Ta doping suppresses grain growth along the a-b plane, leading to the noteworthy outcome of smaller grain sizes. However, with increasing sintering temperature, there is a noticeable facilitation in the formation of larger grains or platelets, as evidenced in Figure 6.8 (d), albeit accompanied by increased non-uniformity.

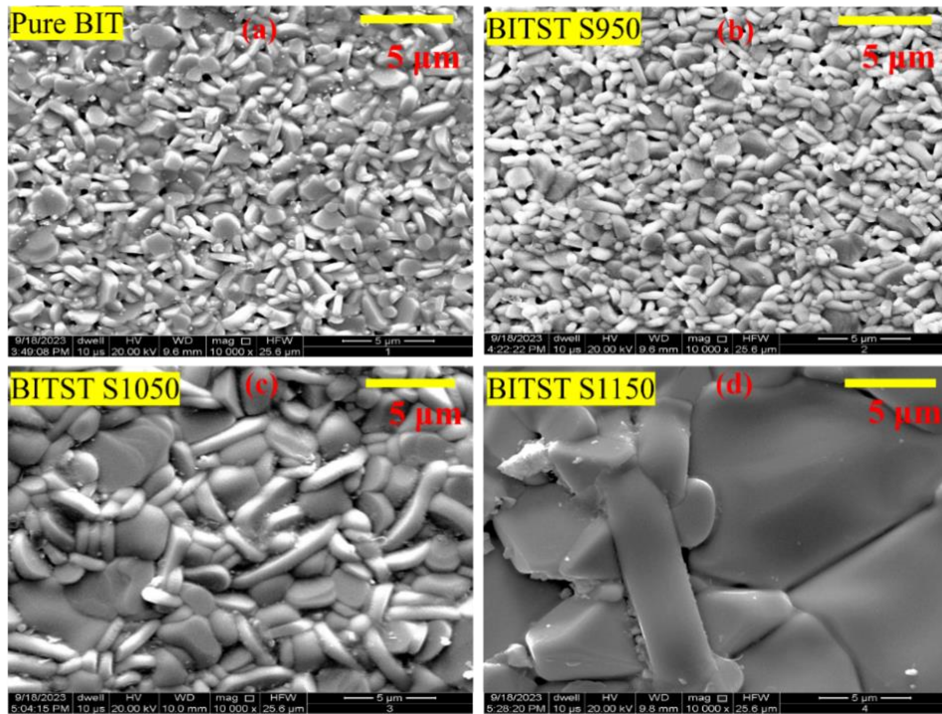

Figure 6.8 SEM micrographs of fractured surface for (a) Pure BIT, (b) BITST S950, (c) BITST S1050 and (d) BITST S1150.

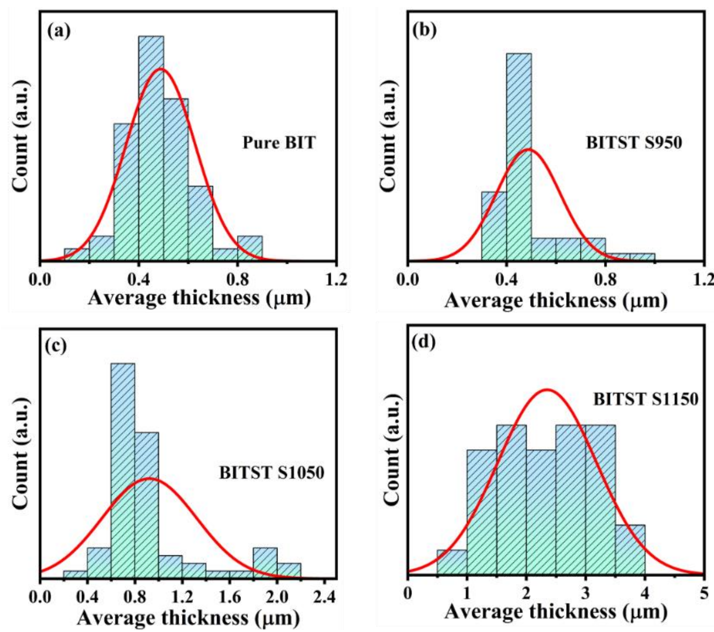

Figure 6.9 Average thickness of the platelet like microstructure of (a) Pure BIT, (b) BITST S950, (c) BITST S1050 and (d) BITST S1150.

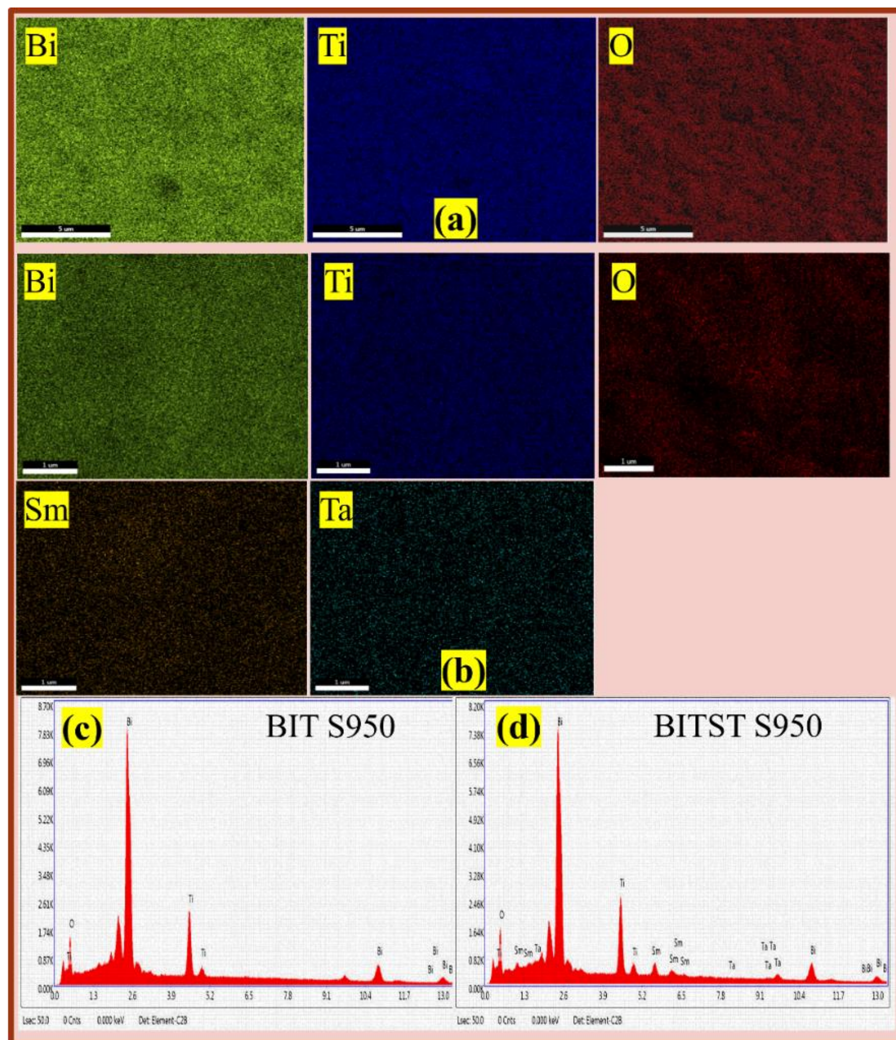

Figure 6.10 Elemental mapping and EDAX of (a,c)Pure BIT and (b,d) BITST S950.

Moreover, larger grain sizes reduce the presence of non-ferroelectric phases at grain boundaries and promote better alignment of domains, leading to improved piezoelectric activity [287].

6.3.3 Ferroelectric Studies

Figure 6.11 depicts the room temperature ferroelectric hysteresis (P-E) loops for (a) Pure BIT, (b) BITST S950, (c) BITST S1050 and (d) BITST S1150 measured at both 10 Hz and 50 Hz. There have been reports of unsaturated PE loops for BIT in previous studies [288], [289]. In pure BIT, as the frequency increases from 10 Hz to 50 Hz, the remnant polarization (P_r) values decrease from 3.7 μC/cm^2 to 1.7 μC/cm^2 at an applied field of 50 kV/cm, and the PE loops become less lossy. This phenomenon could be attributed to the fact that at lower frequencies, vacancies and defects also contribute to the overall polarization, resulting in a seemingly lossy nature. The coercive field of BLSF piezoelectric ceramics is typically high, presenting challenges in achieving complete polarization and consequently resulting in poor piezoelectric performance. For instance, Pure BIT ceramics exhibit a coercive field (E_c) exceeding 60 kV/cm, rendering polarization challenging [250]. In BITST S950 and BITST S1050, the P_r values decrease from 29 to 13 μC/cm^2 and 0.34 to 0.21 μC/cm^2 respectively at an applied field of 50 kV/cm. With an increase in frequency from 10 to 50 Hz, the P-E loops become more rectangular in BITST S950, whereas they become slimmer in BITST S1050. Previous studies have demonstrated that the incorporation of higher-valent cations into BIT effectively reduces oxygen vacancies and vacancy complexes, resulting in a notable increase in P_r values. Furthermore, the lossy nature of P-E loops at lower frequencies suggests the presence of oxygen vacancies and/or defects. Upon further increasing the sintering temperature to 1150 °C, the P-E loops become more slimmer, with P_r values of 0.13 and 0.11 μC/cm^2 at 10 Hz and 50 Hz, respectively, at an applied field of 50 kV/cm. The P-E loops obtained for BITST S1150 were found to be independent of frequency, indicating a reduced contribution of oxygen vacancies to

the net polarization. This observation aligns with the findings from XPS analysis of oxygen vacancies and leakage current measurements.

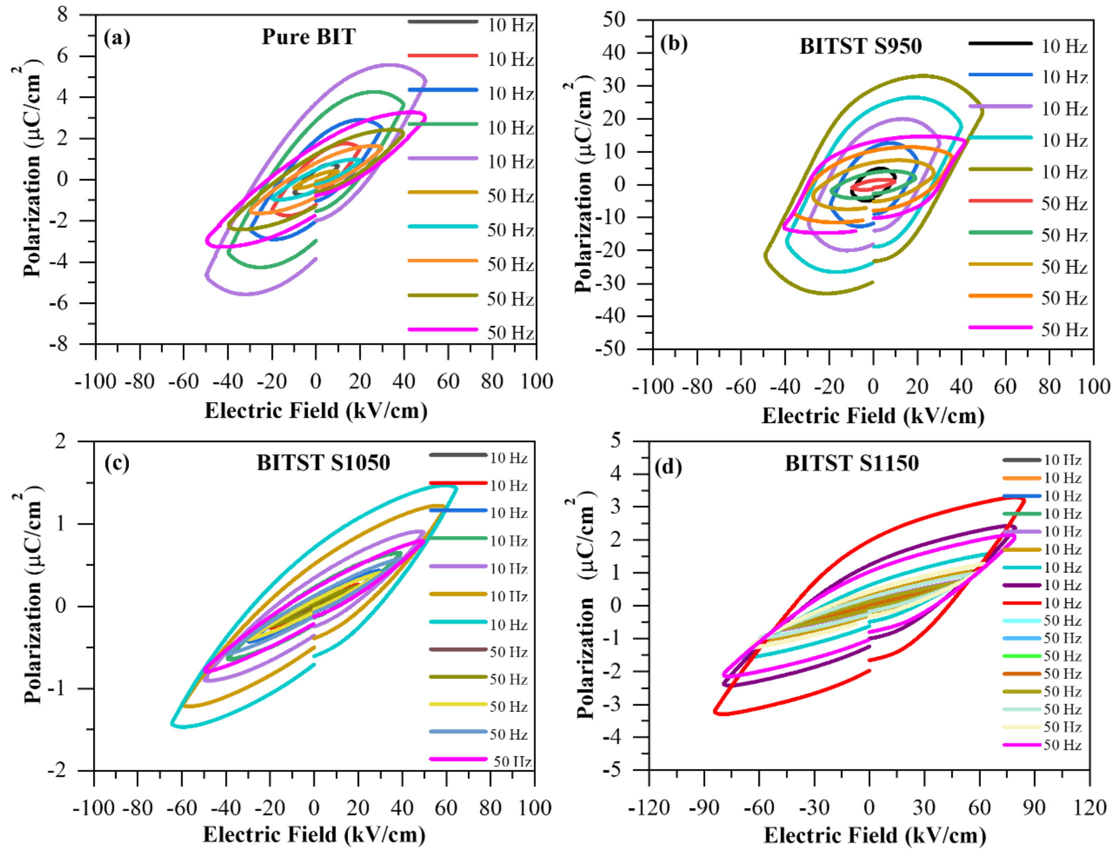

Figure 6.11 Polarization vs Electric field hysteresis loops for (a)Pure BIT, (b) BIT S950, (c) BIT S1050 and (d) BITST S1150.

Figure 6.12 depicts distinct behaviors of the polarization-electric field (P-E) loops at frequencies of 10 Hz and 50 Hz. In Figure 6.12 (a), the P-E loop, characterized by a lossy elliptical shape at 10 Hz, exhibits significant polarization lag relative to the electric field. This elongation diminishes as the frequency increases to 50 Hz, indicative of elevated dielectric relaxation times at the lower frequency. This suggests that the material's polarization mechanisms may be slower to respond at lower frequencies, possibly due to artifacts and defects. Conversely, Figure 6.12 (b) reveals a transition from a more lossy elliptical loop at 10 Hz to a tighter, almost rectangular shape at 50 Hz. This change

signifies a quicker realignment of the polarization with the electric field changes at higher frequencies, pointing to a material with a faster dipolar response and reduced phase lag at increased frequencies. In Figure 6.12 (c), the elongation of the PE loop is relatively stable across the two frequencies, with only a subtle modification in the aspect ratio.

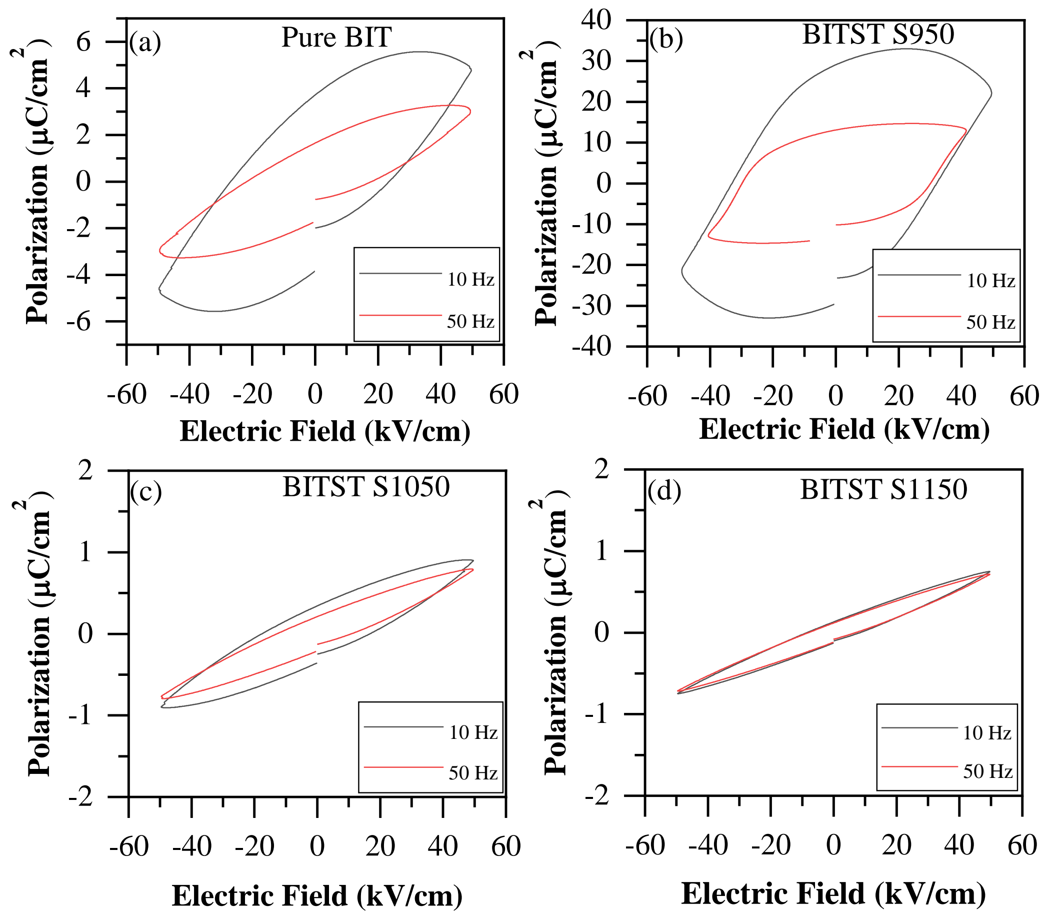

Figure 6.12 Comparison of PE loops at 10 Hz and 50 Hz for (a) Pure BIT, (b) BITST S950, (c) BITST S1050 and (d) BITST S1150.

This consistency implies a stable phase lag regardless of frequency change, suggesting that the polarization response of the material remains largely unaffected by changes in frequency, a characteristic typically associated with materials having stable dielectric properties under varying operational conditions. Finally, Figure 6.12 (d) demonstrates almost negligible change between the loops at 10 Hz and 50 Hz, with the polarization

following the electric field almost instantaneously, represented by the linearity of the loops at both frequencies. This indicates an extremely low dielectric relaxation time, typical of materials with very quick polarization dynamics. These varied responses at different sintering temperatures suggest that the materials demonstrate distinct polarization behaviors under different frequency conditions. This is instrumental in understanding their suitability for applications where frequency response and dielectric stability are critical. Such insights are vital for the design and optimization of electronic components that rely on precise dielectric properties.

Understanding the dynamics of polarization switching in ferroelectric ceramics is vital for optimizing their performance in various applications. Switching peaks observed in current response loops signify reversible electric-field-induced ferroelectric phases within the material. Conversely, the absence of switching peaks suggests either non-ferroelectric behavior or insufficient conditions for polarization switching. To validate the ferroelectric nature and saturation of P-E loops, current measurements were conducted for all samples at 50 Hz, given the lossy nature of P-E loops at 10 Hz. Switching peaks directly correlate with the E_c of ferroelectric materials, representing the electric field strength necessary to induce polarization switching. Identifying the voltage or electric field corresponding to these peaks facilitates the determination of E_C, enabling precise characterization of ferroelectric properties. In BITST S950 and BITST S1150 as shown in Figure 6.13 (b and d), switching peaks were observed at 30 kV/cm and 43 kV/cm, respectively, indicating the value of the E_c. When analyzing current response loops in ferroelectric materials, the presence and characteristics of switching peaks serve as crucial indicators of the material's behavior under an applied electric field. Specifically, the occurrence of two switching peaks within a current response loop signifies the presence of multiple reversible electric-field-induced ferroelectric (FE) phases within the material.

Each of these peaks corresponds to the polarization switching of distinct ferroelectric phases, suggesting the coexistence of different domains or phases with varying polarization orientations or configurations. This complexity in the current response loop indicates the intricacies of the ferroelectric material's domain structure and implies the possibility of distinct polarization switching mechanisms occurring within the sample. Understanding and controlling these multiple ferroelectric phases are essential for tailoring the material's properties to suit specific applications and optimizing its overall performance. Several factors could contribute to the absence of switching peak in Pure BIT and BITST S1050 as shown in Figure 6.13 (a and c), including the material's inherent properties, inadequate measurement conditions such as insufficient voltage or field strength, temperature effects below critical transition points, or the presence of structural defects or impurities hindering polarization switching. Furthermore, the position of a switching peak provides insights into the E_c of the ferroelectric material. E_c represents the electric field strength required to induce polarization switching, and the switching peak marks the point where the applied electric field overcomes this threshold.

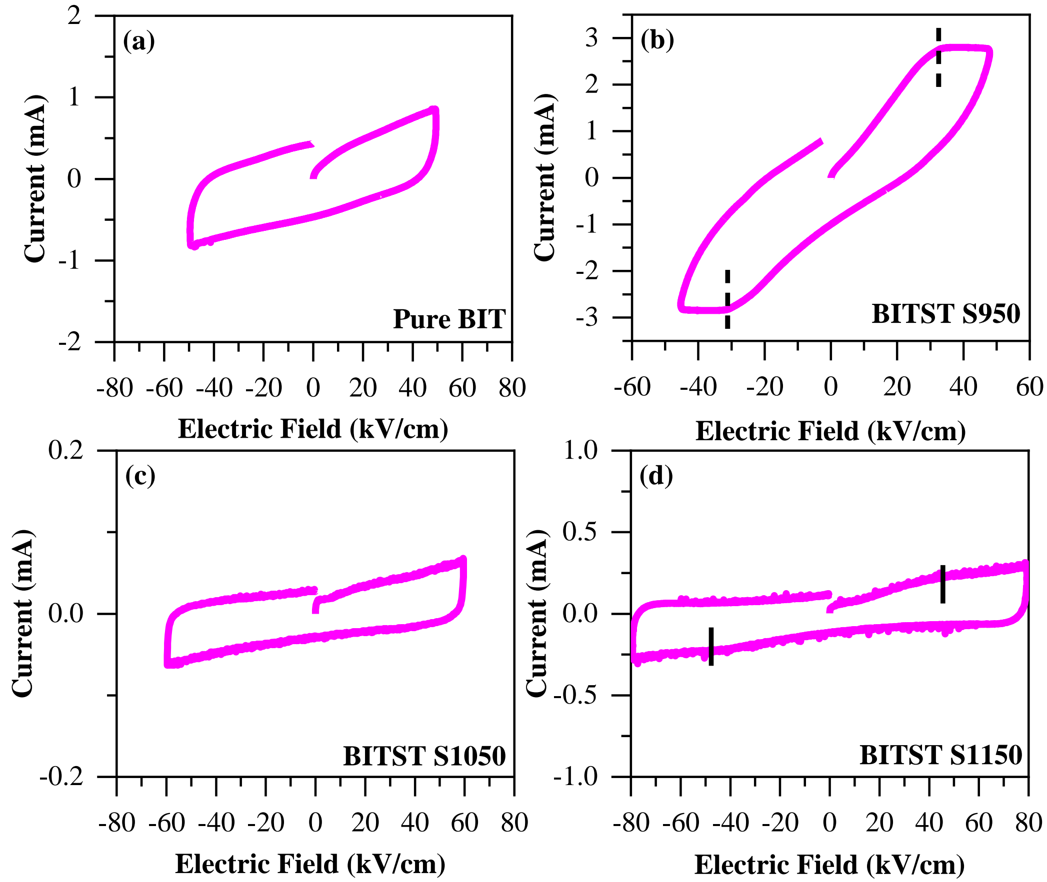

Figure 6.13 Current response loops for (a)Pure BIT, (b) BIT S950, (c) BIT S1050 and (d) BITST S1150 measured at 50Hz.

To further investigate sample resistivity, leakage measurements were conducted, as illustrated in Figure 6.14. For Pure BIT, the resistivity order (Ωcm) was measured to be approximately 10^5, which increases 100 times upon incorporating Sm and Ta into the BIT lattice, reaching 10^7. Furthermore, with the sintering temperature raised to 1150 °C, the resistivity elevated to 10^{10}. These findings are consistent with the outcomes of the ferroelectric and XPS analysis. The observed trends can be attributed to the larger platelet size and improved density, leading to a reduction in oxygen vacancies in BITST S1150. Both bismuth vacancies $(V_{Bi}^{'''})$, and oxygen vacancy defects $(V_O^{\bullet\bullet})$, are formed during high temperature thermal treatment due to the volatilization of Bi_2O_3. The reduction in the concentration of oxygen vacancies is facilitated by the donor dopant function of Ta^{5+}

substitution for Ti^{4+} and Sm^{3+} for Bi^{+3}. This decrease is speculated to be the primary cause of the resistivity increase that occurs after Ta^{5+} doping in BIT ceramics [250]. Electrical conduction along the a-axis in BIT at high temperatures is primarily influenced by oxygen vacancies ($V_O^{\bullet\bullet}$) which are generated through charge compensation involving Bi vacancies (V_{Bi}''') resulting from the volatilization of Bi_2O_3 (Equation 6.1) [250], [273], [274], [290], [291], [292]. As the material cools to room temperature, it gradually oxidizes, resulting in a reduction in the $V_O^{\bullet\bullet}$ concentration while holes $h^{\bullet}$are formed, as depicted by Equation 6.2 [293].

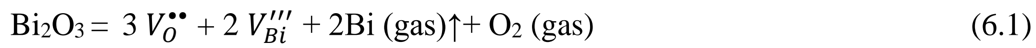

$$Bi_2O_3 = 3\,V_O^{\bullet\bullet} + 2\,V_{Bi}''' + 2Bi\ (gas)\uparrow + O_2\ (gas) \quad (6.1)$$

$$\frac{1}{2}O_2 + V_O^{\bullet\bullet} \rightarrow O_O^{x} + 2h^{\bullet} \quad (6.2)$$

$$Ta_2O_5 \xrightarrow{2TiO_2} 2Ta_{Ti}^{\bullet} + 4O_O^{x} + 2e' + \frac{1}{2}O_2 \quad (6.3)$$

$$Ta_2O_5 + V_O^{\bullet\bullet} \xrightarrow{2TiO_2} 2Ta_{Ti}^{\bullet} + 5O_O^{x} \quad (6.4)$$

The substitution of Ta^{5+} for Ti^{4+} in BITST, according to charge compensation principles, generates two $Ta_{Ti}^{\bullet}$ ions and two free electrons, as outlined in Equation 6.3. This introduction of electrons likely leads to a decrease in the concentrations of both oxygen vacancies and holes, contributing to the observed reduction in electrical conductivity in BITST ceramics. Consequently, electrical conductivity is primarily facilitated by oxygen vacancies at higher temperatures, while hole conduction becomes predominant at lower temperatures. This results in an ionic conduction mechanism at elevated temperatures and a mixed ionic-p-type conduction mechanism at lower temperatures [294]. Additionally, the incorporation of the donor dopant Ta_2O_5 has the potential to eliminate oxygen vacancies, as depicted in Equation 6.4, by neutralizing holes with electrons. This mechanism may partially explain the observed enhancement in resistivity in BITST ceramics [290].

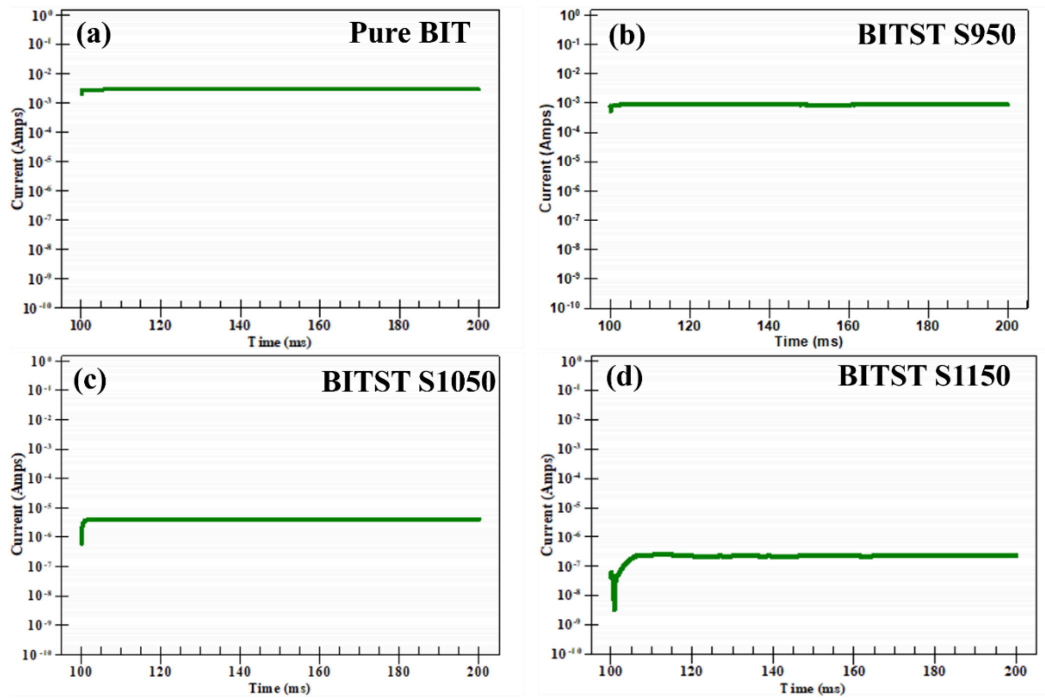

Figure 6.14 Leakage current measurement for (a)Pure BIT, (b) BIT S950, (c) BIT S1050 and (d) BITST S1150 measured at 50kV/cm at 50Hz.

The Positive Up Negative Down (PUND) method involves conducting pulsed measurements. This technique enables the differentiation between the switchable and non-switchable components of polarization. Figure 6.15 (a-b) illustrates the PUND voltage profile, displaying five distinct pulses. The measurement entails the transmission of a series of five pulses. Initially, a preset pulse (referred to as Pulse 1) is dispatched to establish the sample's polarization in a specific direction.

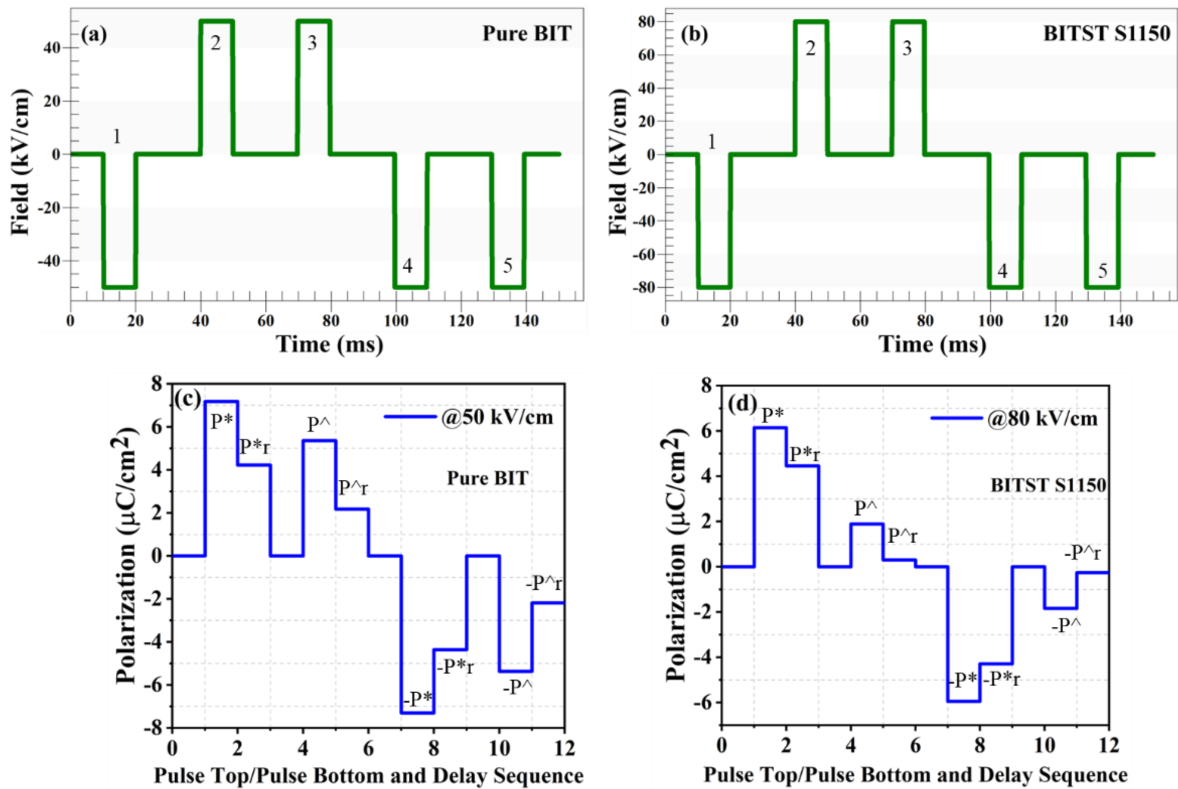

Figure 6.15 PUND voltage profile and resulting output curve corresponding to pulse width and pulse delay of 10 ms for (a, c) pure BIT, (b, d) BITST S1150, respectively.

Subsequently, Pulse 2 is administered to reverse the polarization. Pulse 3 follows, applying field in the same direction as Pulse 2, thereby not affecting the sample's polarization. Lastly, Pulse 4 and Pulse 5 mirror the actions of Pulses 2 and 3 but in the opposite direction. In Figure 6.15 (c-d), P* is the value of polarization at maximum applied field (E_{max}) during the Pulse 2. This represents a switching pulse and the value contains remnant + non-remnant polarization components. P*r is the value of polarization measured at 0 Volts after the second pulse and the PUND delay time. P^ is the value of polarization measured at maximum applied field (E_{max}) during the Pulse 3. This represents a non-switching pulse and the value contains only non-remnant polarization components. P^r is the value of polarization measured at 0 Volts after the third pulse and the PUND delay time. The polarization results obtained as a result of applying different electric field

during PUND cycles are shown in Figure 6.16 (a-b) corresponding to the pulse 2, 3, 4 and 5. In Figure 6.16, ΔP, ΔPr, -ΔP and -ΔPr denotes the sample remnant polarization where ΔP=P*-P^, ΔPr=P*r-P^r, -ΔP=-P*-(-P^) and -ΔPr=-P*r-(-P^r). In the case of BITST S1150, the remnant polarization values, including ΔP, ΔPr, -ΔP, and -ΔPr, are significantly higher compared to those of pure BIT. This improvement can be attributed to several factors: lower oxygen vacancies, reduced leakage current, increased resistivity, and enhanced density of the BITST S1150 samples. Oxygen vacancies, which carry positive charges, typically accumulate at domain walls, impeding their mobility and thus hindering efficient switching. However, by reducing these oxygen vacancies, the domain walls experience less pinning, which facilitates more effective switching. This adjustment leads to enhanced remnant polarization, higher dielectric constant, and improved d_{33} values. Furthermore, previous studies have shown that substituting higher valence cations at the B-site effectively compensates for defects that contribute to fatigue phenomena and domain pinning. Building on this, A/B site engineering with Ta and Sm doping in BIT has the potential to further reduce defects, thereby significantly enhancing the ferroelectric properties.

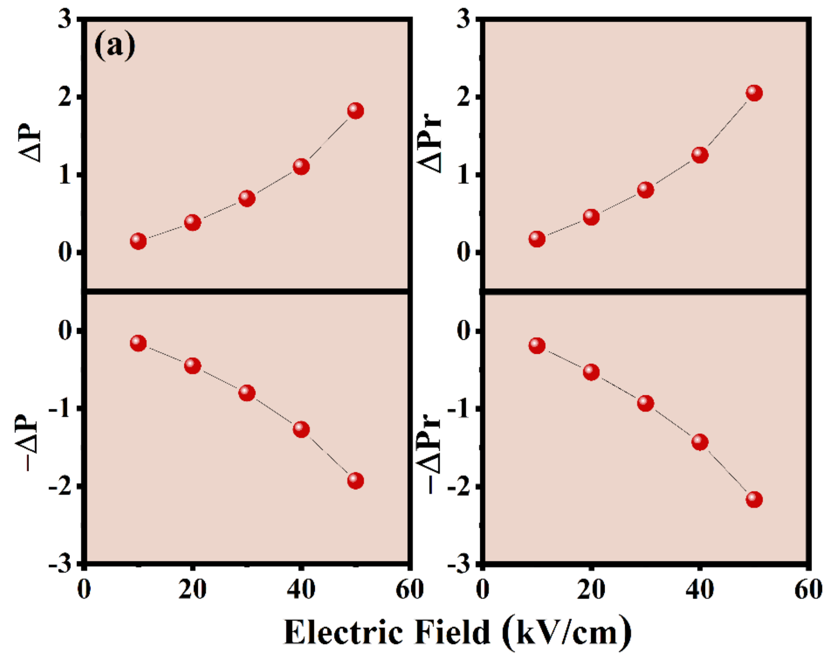

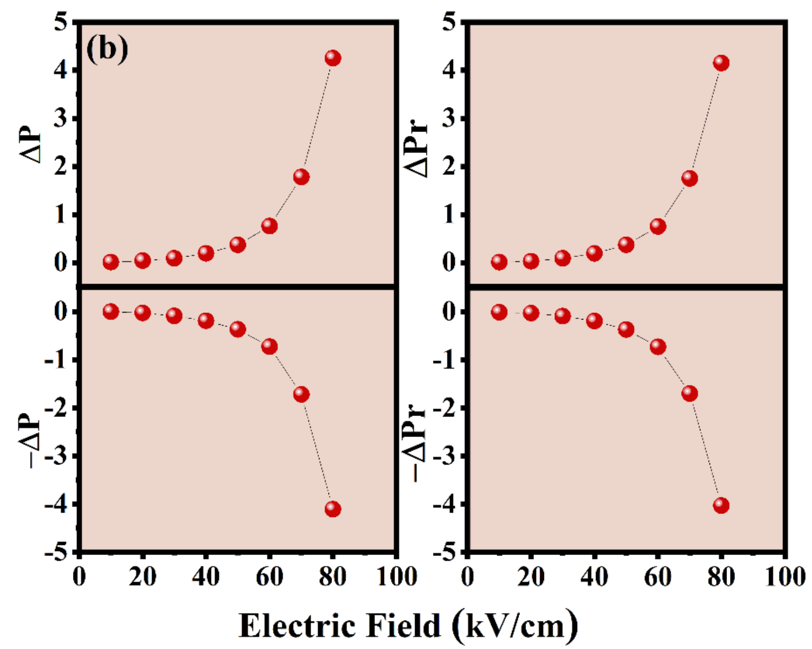

Figure 6.16 PUND remnant polarization in four cycles for (a) Pure BIT and, (b) BITST S1150.

6.3.4 Dielectric and Piezoelectric Studies

Figure 6.17 (a-b) displays the temperature-dependent dielectric constant (dielectric permittivity, ε_r) and dielectric loss (tan δ) plots for all the prepared compositions measured at 10 kHz, respectively. The peak corresponding to the maxima of dielectric constant curve provides the T_C of around 674 °C for pure BIT and subsequently 594 °C, 597 °C, 617 °C for BITST S950, BITST S1050, and BITST S1150, respectively. The substitution of Ta^{+5} for Ti^{4+} in BIT leads to decrement in the T_C, a phenomenon observed similarly with Nb^{5+} and Ta/Nb doping in previous studies [291], [295]. However, upon increasing the sintering temperature of BITST from 950 °C to 1150 °C, the value of T_C shifts to higher temperatures. Additionally, the dielectric constant corresponding to T_C increases from 1075 to 4236 as the sintering temperature rises from 950 °C to 1150 °C in BITST. The Rietveld analysis revealed that the introduction of Ta^{5+} ions, with a larger radius of 0.64 Å, into BIT ceramics, substituting for Ti^{4+} ions with a smaller radius of 0.605 Å, induces distortion in the TiO_6 octahedra and reduces barriers. This distortion leads to a decrease in free energy, resulting in a reduction in the T_C of the ceramics [296]. This phenomenon can be attributed to the increase in dielectric constant due to the heightened polarizability resulting from the distortion of oxygen octahedra caused by the substitution of Ta at the B site [297]. Alternatively according to previous reports the reduction in Tc can be attributed to substitution of Ti^{4+} with transition metal ions featuring higher nd0 electron orbits like 5d orbital of Ta^{5+} as opposed to 3d orbital of Ti^{4+} [250]. The dielectric loss values at room temperature for pure BIT, BITST S950, BITST S1050, and BITST S1150 are 0.21, 0.06, 0.05, and 0.04, respectively. The reduction in the loss tangent values is attributed to higher-valent cation doping, which aids in reducing space charge density, minimizing oxygen vacancies, and suppressing polarization pinning [277], [297].

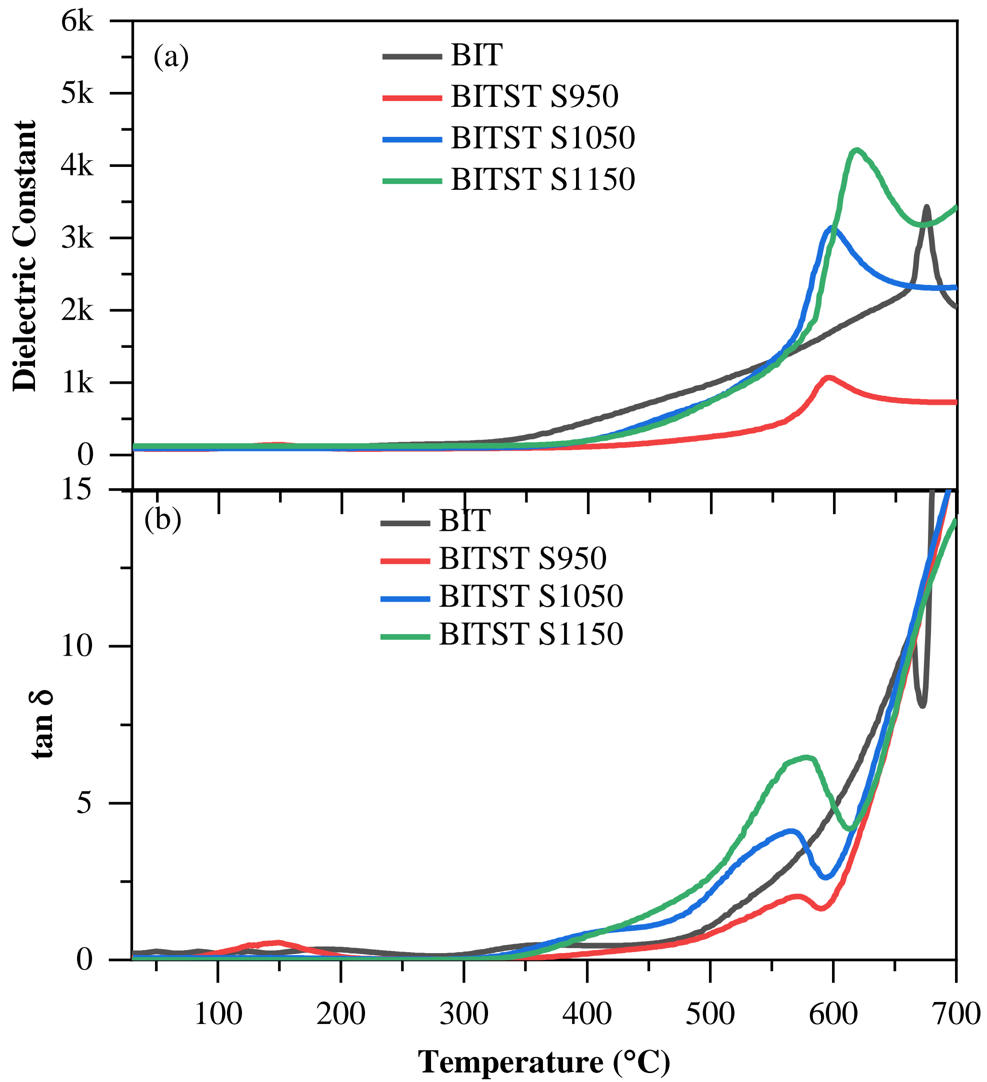

Figure 6.17 Temperature dependent (a) dielectric constant and (b) dielectric loss (tan δ) for BIT, BITST S950, BITST S1050, BITST S1150 measured at 10 kHz.

The dielectric loss remains below 1 over a wide range of temperature, up to 400 °C which makes it suitable for high temperature applications. The incorporation of Ta^{5+} ions at the B-site in BIT as donor impurities effectively reduces oxygen vacancies, a phenomenon explained by the defect reaction:

$$Ta_2O_5 + V_O^{\bullet\bullet} \rightarrow 2Ta_{Ti}^{\bullet} + 5O_O^{x} \qquad (6.5)$$

This reduction in oxygen vacancies due to Ta^{5+} doping leads to a decrease in the dielectric loss peak, consistent with previous findings [291]. The migration of positively charged oxygen vacancies toward domain walls with lower potential energy impedes the switching of domains. Decreasing the concentration of oxygen vacancies diminishes the pinning effect on domain walls and augments the number of accessible switching domain walls, thereby improving remnant polarization, dielectric constant, or d_{33} [298].

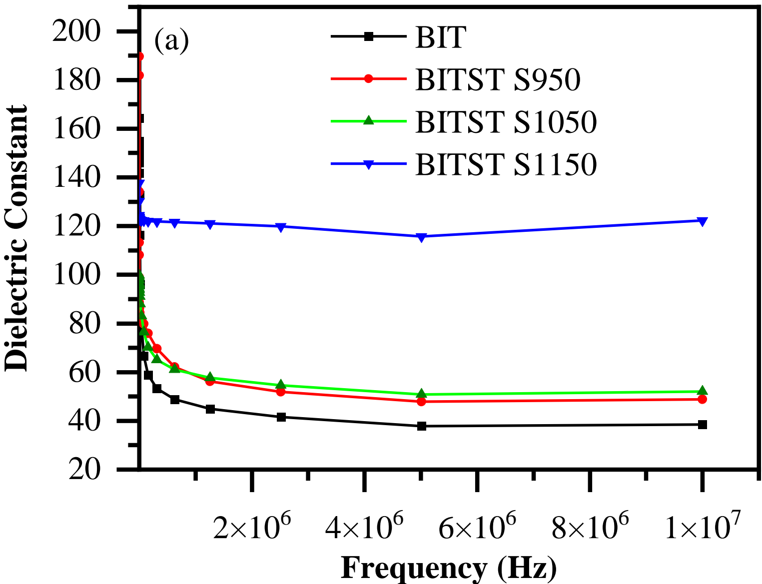

Figure 6.18 Frequency dependent dielectric constant curves for BIT, BITST S950, BITST S1050, and BITST S1150 at 100 °C.

The substitution of Sm/Ta in BIT results in suppression of defects and vacancies caused by the volatization of Bi at higher temperatures [267], [299]. The higher dielectric constants found at low frequencies could be attributable to the Maxwell-Wagner contribution. Space charge polarization, arising from oxygen vacancies, contributes to the dielectric response at lower frequencies. However, as the frequency increases, the dielectric constant decreases because the dipoles are unable to realign rapidly with the applied electric field at higher frequencies. At higher frequencies, internal friction

increases, leading to energy dissipation as heat. This dissipation reduces the material's ability to retain electric charges, resulting in a decrease in the dielectric constant. The dielectric loss decreases with increasing frequency, indicating that defects have difficulty aligning themselves with the applied field, thus contributing primarily at lower frequencies. The rise in tan δ at low frequency and elevated temperature is primarily attributed to loss stemming from conductivity. Moreover, the presence of Sm^{3+}/Ta^{5+} ions suppress the volatilization of Bi and diminishes defects, resulting in an enhancement of dielectric constant and reduction of dielectric losses. BITST S1150 exhibits the lowest dielectric losses, while pure BIT displays the highest, underscoring the efficacy of Sm/Ta substitution in reducing leakage current, enhancing resistivity, and increasing density. These findings underscore the influence of composition on dielectric properties, suggesting a significant impact of charge defects and oxygen vacancies on dielectric response. Figure 6.19 illustrates the variation of the piezoelectric charge coefficient (d_{33}, pC/N) across the different compositions under optimized poling conditions. The d_{33} values exhibit an increase from 7 pC/N for pure BIT to an enhanced value of 39 pC/N for BITST S1150, trend similar to previous studies [300]. The improvement in piezoelectric characteristics may be ascribed to the distortion of TiO_6 octahedra, which facilitates domain mobility [296]. The impact of poling conditions on piezoelectricity is indeed substantial. The need for a relatively lower poling field of 20-25 kV/cm for pure BIT pellets is likely due to their high leakage characteristics resulting from poor density and oxygen vacancies. These factors contribute to a lower d_{33} value [298]. However, the d_{33} values increased to 13, 25, and 39 pC/N with the increment in sintering temperature for Sm/Ta co-doped BIT from 950 °C to 1150 °C, respectively. The incorporation of Sm/Ta and the subsequent increase in sintering temperature led to an increase in the d_{33} value. This improvement can be ascribed to various factors, including higher density, larger

grain size, and enhanced electrical insulating properties resulting from the reduction in the concentration of oxygen vacancies. The d_{33} and T_C values obtained in this study (d_{33} ~39 pC/N, T_C ~617 ◦C) were evaluated against previously reported data, confirming the remarkable characteristics of the BITST S1150 piezoceramic specimen [271], [272], [273], [274], [291], [298], [301], [302], [303], [304].

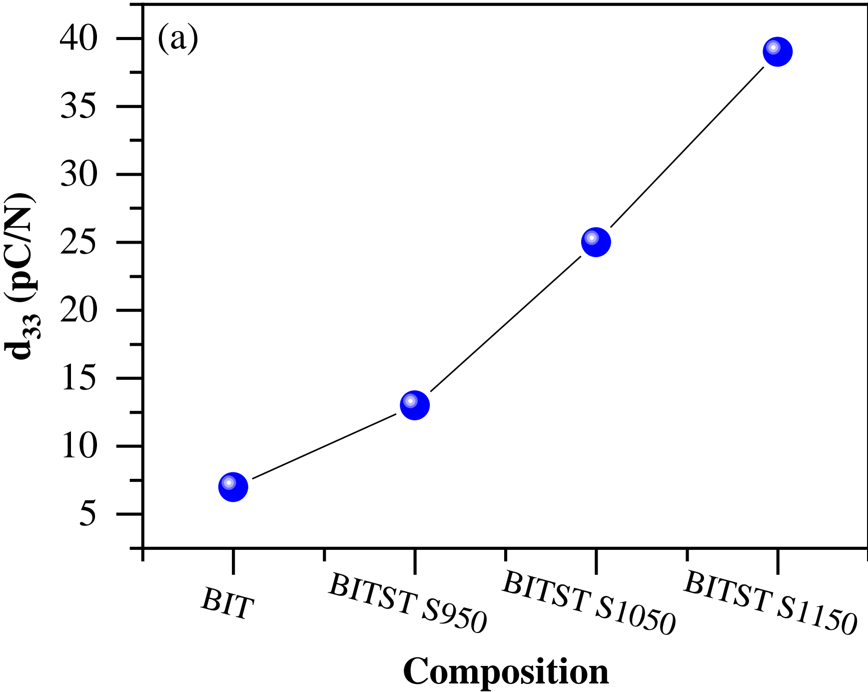

Figure 6.19 Piezoelectic charge coefficient (d_{33}) for BIT, BITST S950, BITST S1050, and BITST S1150.

Table 6.2 lists data on the piezoelectric charge coefficient (d_{33}) and Curie temperature (T_C) for variously doped BIT-based compounds. An inverse correlation between T_C and d_{33} necessitates meticulous fine-tuning to optimize the balance between high piezoelectric responsiveness and thermal stability. Among these materials, BITST S1150 ceramics standout due to their remarkable piezoelectric coefficient, with d_{33} values reaching approximately 39 pC/N, coupled with an elevated resistivity of 10^{10} Ωcm, and a comparatively high Curie temperature of around 617°C. This exceptional combination

suggests a meticulous material engineering strategy where an increase in piezoelectric activity has been achieved, albeit at the cost of a slightly reduced T_C.

Table 6.2 Piezoelectric charge constant and Tc values of different BIT based compounds.

Materials/doping	d_{33} (pC/N)	T_C	Ref.
Pure BIT	7	675	[274]
BIT-W	16	652	[274]
BITW-Mn	21	655	[274]
BIT-Nb	20	655	[273]
BIT-Nb/Ta	39	690	[298]
$Bi_4Ti_{2.98}Nb_{0.01}Ta_{0.01}O_{12}$	26	668	[291]
BIT-W/Nb	32	655	[272]
BIT-Cu/Sb	24	672	[302]
$Bi_{3.97}Ce_{0.03}Ti_{2.98}(WNb)_{0.01}O_{12}$	40.2	657	[271]
$Bi_4Ti_{2.9}W_{0.05}Nb_{0.05}O_{12}$	22.8	635	[300]
$Bi_{3.96}Ce_{0.04}Ti_{2.97}W_{0.015}Nb_{0.015}O_{12+\delta}$	34.3	643	[244]
$Bi_4Ti_{2.96}W_{0.02}Cr_{0.02}O_{12}$	31.1	651	[304]
$Bi_4Ti_{3-x}(Cu_{1/3}Sb_{2/3})_xO_{12}$ (x=0.035)	24	672	[302]
$Bi_4Ti_{2.95}(Mg_{1/3}Nb_{2/3})_{0.05}O_{12}$	30	685	[305]
$Bi_4Ti_{2.95}(Mg_{1/3}Nb_{2/3})_{0.05}O_{12}$	20	686	[303]
$Bi_4Ti_{3-x}(Mn_{1/3}Ta_{2/3})_xO_{12}$(x = 0.01)	31	684	[250]
$Bi_4Ti_{3-x}(Cu_{1/3}Ta_{2/3})_xO_{12}$ (x=0.015)	34	677	[290]
$(Bi_{4-x}Sm_{0.5})(Ti_{3-0.01}Ta_{0.01})O_{12}$	39	617	This work

However, the elevated T_C still supports high-temperature applications, making this

composition highly suitable for environments where thermal resilience and piezoelectric efficiency are paramount. Moreover, BITST S1150 ceramics also exhibit a broad sintering window, enhancing their manufacturability and durability. This feature, along with their superior piezoelectric properties, positions these ceramics as a promising candidate for advanced applications that demand robust high-temperature piezoelectric materials. The interplay of these characteristics underscores the importance of optimizing material compositions to achieve desired outcomes, aligning the technological demands with the intrinsic material properties.

6.3.5 Optical Properties Studies

The Kubelka- Munk plots obtained from the UV-Vis DRS characterization of pristine BIT, BITST S950, BITST S1050, and BITST S1150 are depicted in Figure 6.20 (a-d). The Kubelka Munk function $F(R)$ *is* given by: $F(R)=(1-R)^2/2R$, where R is the reflectance, transforms reflectance into a form similar to the absorption coefficient (A). To find the optical band gap of the material, the Kubelka-Munk function is usually plotted against photon energy ($h\nu$) in a format known as the Tauc plot given by equation $(F(R).\ h\nu)^n = A\ (h\nu - E_g)$, where n=1/2 (indirect) and 2 (direct). The indirect band gap (E_g) reduces from 3.11 eV obtained for pure BIT to 3.06 eV for Sm/Ta substituted BIT sintered at 1150 °C, which is within the range calculated theoretically [306]. The reduction of the band gap on increasing the sintering temperature and on incorporation of doping can be attributed to the emergence of sub-bands created by Sm/Ta and oxygen vacancies between the valence band maxima and the conduction band minima. The $Bi_4Ti_3O_{12}$ structure, comprising intergrown perovskite and fluorite units, features three layered blocks of $Bi_2Ti_3O_8$ with a net charge of +2 and fluorite bilayer blocks Bi_2O_4 with a net

charge of −2. This arrangement brings band edges closer, narrowing the band gap, crucial for electronic structure. Positively charged regions repel cations, lowering the conduction-band edge, while negatively charged regions repel anions, raising the valence-band edge, thus stabilizing the well-ordered intergrowth structure [306]. Oxygen vacancies also plays a significant role in lowering the conduction band tail. The slight hump with smaller slope is obtained on the lower energy region of Kubelka-Munk Tauc plot for the doped samples (see Figure 6.20 (b-d)) the obtained band gap from the threshold can be termed as E_{g1}, which is lower than the real optical band gap (E_g). The values obtained for Eg_1 are 2.74 eV, 2.81 eV, 2.83 eV in BITST S950, BITST S1050, BITST S1150, respectively.

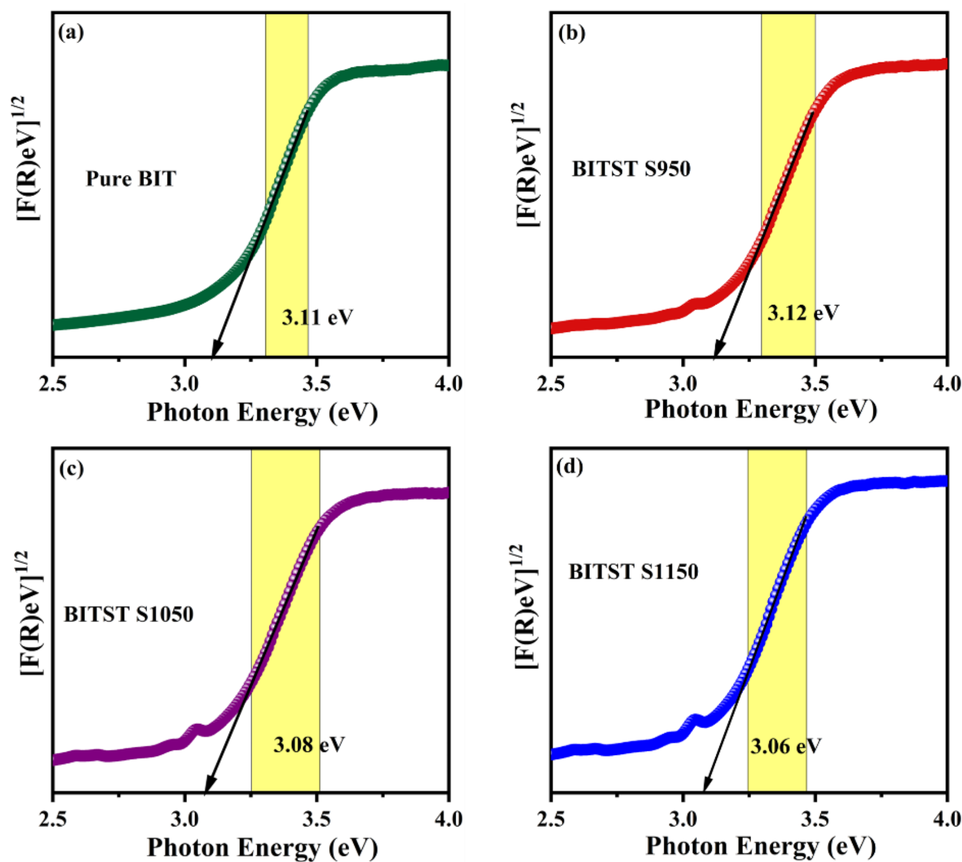

Figure 6.20 Band gap calculation using Kubelka-Munk function Vs. Photon Energy plot for Pure BIT, BITST S950, BITST S1050 and BITST S1150 obtained from UV-Vis diffuse reflection spectroscopy.

The photoluminescence characteristics of BIT were studied by recording the excitation spectrum while monitoring the emission at 600 nm as depicted in Figure 6.21 (a). A sharp and intense excitation band centered at 404 nm was observed. Subsequently, photoluminescence spectra were recorded for BIT, BITST 950, BITST 1050 and BITST 1150 in the range of 550–680 nm under this excitation wavelength as illustrated in Figure 6.21 (b). These spectra exhibit three emission bands centered at 565, 601 and 649 nm corresponding to the $^4G_{5/2}\rightarrow{}^6H_J$ (J=5/2, 7/2, 9/2) transitions, respectively. The emission transitions noted include the $^4G_{5/2}\rightarrow{}^6H_{9/2}$ transition, which is exclusively of electric dipole nature ($\Delta J \leq 6$), while the other two transitions ($^4G_{5/2}\rightarrow{}^6H_{5/2,\,7/2}$) involve both electric and magnetic components ($\Delta J=0, \pm 1$).

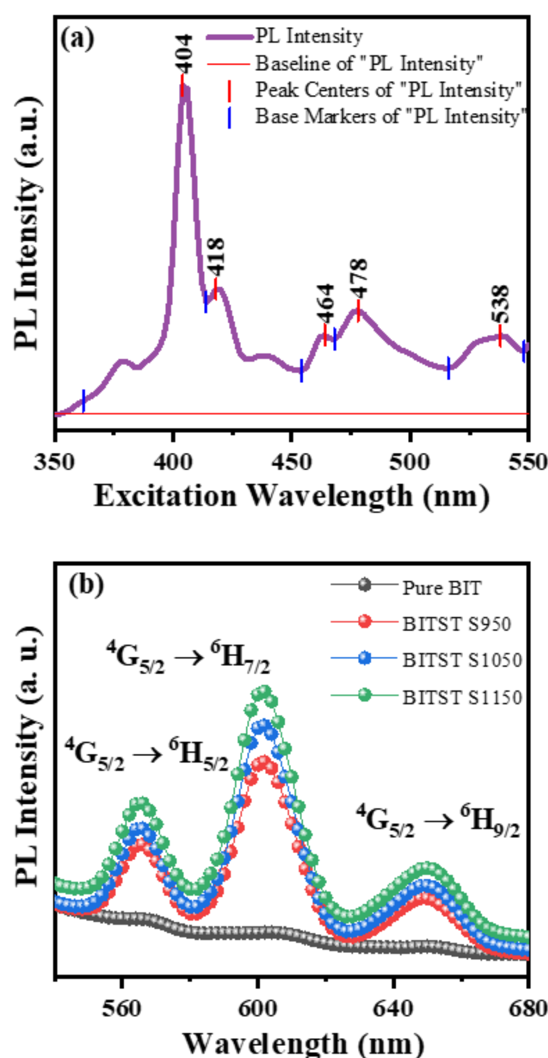

Figure 6.21 (a) Excitation spectra and (b) Emission PL spectra for all the compositions.

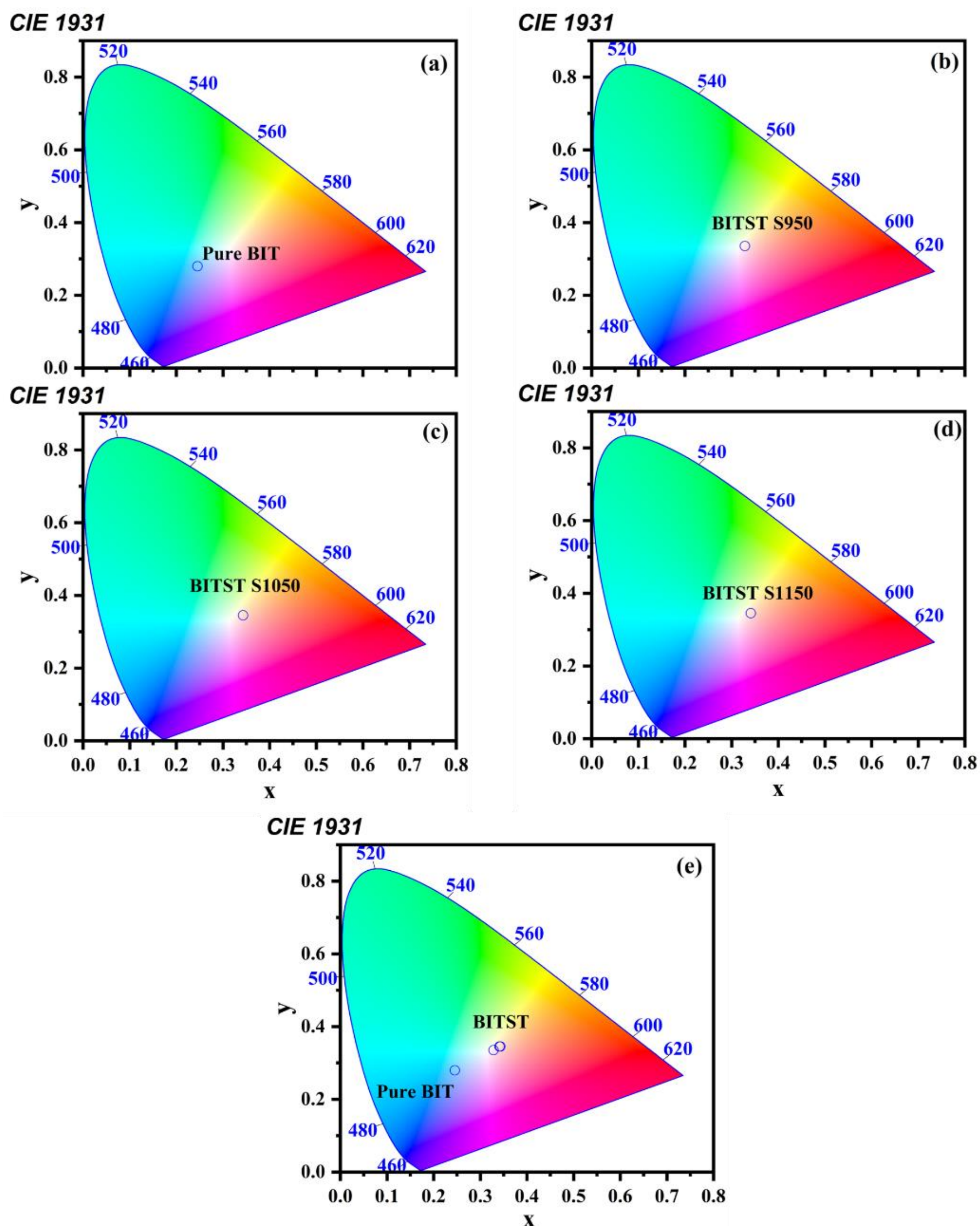

Figure 6.22 CIE color chromaticity diagram showing the wavelength and corresponding colour of emission wavelength (a) Pure BIT, (b) BITST S950, (c) BITST S1050, (d) BITST S1150 and (e) comparison showing effect of Sm, Ta incorporation in BIT.

Among these, the emission band linked to the $^4G_{5/2} \rightarrow {}^6H_{7/2}$ transition exhibits the highest intensity. The luminescence intensity of Sm^{3+} in BITST increases with increasing

sintering temperature, reaching a maximum at 1150 which might be attributed to the higher radiative recombination rates as it facilitates easier electron-hole recombination, potentially increasing PL intensity.

To analyze the emitted color from the samples, the chromaticity coordinates were determined from the emission spectra using the CIE diagram, as shown in Figure 6.22. The intrinsic excitation of the emission spectra has three main components: a segment in the blue region, another segment spanning from orange to red, and a third segment in the green region. The chromatic coordinates of pure BIT (x=0.24, y=0.28) were situated towards the center of the green-blue region. Upon doping, the color coordinates shifted towards the intersection of all three regions, indicating a shift towards higher wavelengths. This shift was evident in BITST S950, BITST S1050, and BITST S1150, with coordinates (x=0.33, y=0.33), (x=0.34, y=0.34), and (x=0.34, y=0.34), respectively, as confirmed by Figure 6.22 (e). This suggests that variations in sintering temperature do not significantly affect the emission color, while the doping of Sm^{3+} causes a shift towards higher wavelength regions.

6.4 Conclusion

This study has successfully analyzed the influence of Sm/Ta co-doping on the functional properties of BIT ceramics across various sintering temperatures. Through strategic A/B site engineering, the dielectric, ferroelectric, and piezoelectric properties of BITST ceramics, particularly those sintered at 1150 °C (BITST S1150), were significantly enhanced. The preparation of dense microstructures in BITST ceramics was achieved through a traditional solid-state reaction approach. Comprehensive characterization employing XRD and FTIR corroborated the formation of a pure phase with a notable

increase in lattice distortion—indicative of the successful incorporation of Sm and Ta into the BIT matrix. This incorporation effectively lowers the concentration of inherent oxygen vacancies, consequently reducing leakage current and enhancing resistivity. The ferroelectric measurement shows that the P-E loops become slim on increasing the sintering temperature indicating reduction in lossy behavior due to increased grain size, density and reduced oxygen vacancies. For instance, BITST S1150 demonstrated a piezoelectric charge coefficient (d_{33}) of 39 pC/N, significantly higher than that of pure BIT, which illustrates a substantial improvement in piezoelectric properties. The BITST S1150 ceramics exhibited an increased T_C (~617 °C), improved dielectric constants up to 4236, and reduced dielectric losses, validating their suitability for high-temperature applications. Notably, the resistivity of the ceramics was markedly enhanced, achieving values as high as 10^{10} Ω.cm for BITST S1150 compared to 10^5 Ω.cm for pure BIT. Additionally, optical property enhancements, including a narrowing of the band gap (3.12 eV to 3.06 eV) and increased luminescence suggest improved light absorption capabilities, facilitating potential applications in optoelectronic devices. In conclusion, the findings elucidate the significant role of dopant selection and sintering temperature in optimizing the microstructural and functional properties of BIT ceramics. This investigation underscores the potential of tailored BITST ceramics for high-performance applications in environments demanding robust electrical and optical properties. Further exploration of these materials could lead to significant advancements in the development of devices capable of operating under extreme conditions, thereby extending the functional limits of piezoelectric and optoelectronic materials.